

10 W 量级高功率中红外超快光纤激光系统中色散管理的仿真设计

孙伟义^{1,5}, 黄家鹏^{1,2,4*}, 陈丽明², 黄志远¹, 何文彬², 江昕^{2,3}, 庞盟^{1,2,3**}, 冷雨欣^{1,3***}

¹中国科学院上海光学精密机械研究所强场激光物理国家重点实验室, 上海 201800;

²中国科学院上海光学精密机械研究所激光技术新体系融合创新中心, 上海 201800;

³国科大杭州高等研究院物理与光电工程学院, 浙江 杭州 310013;

⁴香港理工大学电机工程系, 香港;

⁵上海科技大学物质科学与技术学院, 上海 201210

摘要 超快光纤激光器具有结构紧凑、可靠性高和光束质量好等优点, 在科学研究和工业生产上有广泛的应用。2~5 μm 波段的中红外超快光纤激光器在气体探测、激光手术与中红外对抗中具有巨大的应用潜力, 已成为超快光纤激光器领域的一个研究热点, 尤其是利用掺杂铟离子的氟化物光纤作为增益光纤的光纤激光器, 其可利用常见的 980 nm 泵浦激光产生 2.8 μm 波段的超快激光, 是研究最为广泛的中红外超快光纤激光器系统之一。然而, 2.8 μm 波段的超快光纤激光器无论是在平均功率还是在单脉冲能量上, 都与国际先进的近红外波段超快光纤激光器存在较大差距。前期报道的 2.8 μm 超快光纤激光器输出的最高平均功率约为 1 W, 单脉冲能量约为 30 nJ, 这极大地限制了中红外超快光纤激光在高灵敏度气体测量等领域的应用。针对这一问题, 本文设计了一套基于掺杂铟离子氟化物光纤的多级啁啾脉冲放大系统, 并对其进行了数值模拟, 此系统可将脉冲平均功率放大到 10 W 量级, 从而获得超过 250 nJ 的单脉冲能量。此系统输出的高能量中红外脉冲具有约 400 fs 的超宽脉冲宽度, 脉冲峰值功率可达 450 kW。

关键词 激光器; 中红外激光; 锁模光纤激光器; 啁啾脉冲放大; 高功率脉冲激光

中图分类号 TN212

文献标志码 A

doi: 10.3788/CJL202249.0101012

1 引言

中红外波段激光在材料加工^[1]、激光医疗^[2]、生化传感^[3]、气体探测^[4-5]以及光谱学^[6]上具有巨大的应用价值, 主要原因是在中红外波段存在众多气体分子的振动特征吸收峰, 且吸收强度较近红外波段高出至少一个量级^[7], 因此中红外波段也被称为“分子指纹区”。当下, 常见的中红外波段激光光源主要有量子级联激光器^[8]、自由电子激光器^[9]及基于激光非线性频率转化的中红外产生系统^[10-14]。这些中红外激光产生方法都存在各自的瓶颈: 量子级联激光器波长可调谐, 但一般只能产生皮秒量级脉冲宽度的中红外激光^[15-16]; 自由电子激光输出脉冲能量高, 但是装置

巨大, 造价高昂; 基于非线性频率变换技术的中红外光源, 例如中红外光参量振荡器(optical parametric oscillator, OPO)、光参量啁啾脉冲放大(optical parametric chirped-pulse amplification, OPCPA)系统与差频产生(difference frequency generation, DFG)系统, 结构相对复杂, 调节难度较大。相较于其他中红外激光产生系统, 中红外光纤激光器具有光束质量高、散热性能优异、结构紧凑等优点, 且中红外波段增益光纤具有较宽的增益谱宽度, 通过锁模技术可产生飞秒尺度的超快中红外脉冲激光。

由于石英玻璃在中红外波段的透过率极低, 因此在这一波段需要采用特殊的光纤材料, 例如亚碲酸盐玻璃^[17-18]、氟化物玻璃^[19]、硫系玻璃^[20-21]等。

收稿日期: 2021-10-18; 修回日期: 2021-11-09; 录用日期: 2021-11-15

基金项目: 上海市 2021 年度“科技创新行动计划”原创探索项目(21ZR1482700)、2021 年度博士后创新人才支持计划(BX2021328)、张江实验室建设与运行项目(三期)(20DZ2210300)、国家高层次人才青年项目

通信作者: *jiaphuang@polyu.edu.hk; **pangmeng@siom.ac.cn; ***lengyuxin@siom.ac.cn

其中 ZBLAN ($\text{ZrF}_4\text{-BaF}_2\text{-LaF}_3\text{-AlF}_3\text{-NaF}$) 玻璃光纤具有稀土掺杂浓度高、破坏阈值高、非线性系数较小和材料化学稳定性好等特点,因此利用掺杂铒离子氟化物光纤搭建的 $2.8\ \mu\text{m}$ 光纤激光器在近几年得到了快速发展,例如:加拿大拉瓦尔大学的研究团队实现了 $2.8\ \mu\text{m}$ 、 $40\ \text{W}$ 的连续激光输出^[22];上海交通大学 Qin 等^[23]通过使用非线性偏振旋转(NPR)锁模技术输出了脉冲宽度为 $215\ \text{fs}$ 、能量为 $9.3\ \text{nJ}$ 的脉冲输出;Huang 等^[24]采用色散管理得到脉冲宽度为 $126\ \text{fs}$ 、能量为 $10\ \text{nJ}$ 的脉冲输出。更高平均功率与单脉冲能量的中红外超快光纤激光系统,一方面可提升材料加工与激光手术的效率,另一方面也可以提高气体探测与光谱学测量的精度。因此,在锁模中红外超快光纤激光种子源中,往往会引入光纤放大器来进一步提高中红外超快激光的平均功率与单脉冲能量^[24-26]。然而,之前报道的基于掺杂铒离子氟化物光纤的 $2.8\ \mu\text{m}$ 超快光纤激光器的最高输出功率为瓦量级,单脉冲能量约为 $30\ \text{nJ}$ ^[24]。限制其平均功率与单脉冲能量无法继续提升的根本原因:在超快光纤激光放大器中更高的单脉冲能量会导致过强的非线性效应,导致高能量脉冲放大过程中产生时域分裂与频谱畸变,这将严重影响输出激光脉冲的时间特性与峰值功率。为避免这一问题,最为常用的方法是啁啾脉冲放大(chirped-pulse amplification, CPA)技术^[13]:利用脉冲展宽器在光纤放大器之前引入较大的脉冲啁啾,将飞秒脉冲在时域上拉伸,从而极大地降低光纤放大器中的脉冲

峰值功率,避免较强的非线性效应。尽管 CPA 技术在近红外波段超快光纤激光器上发展已较为成熟,利用此技术的先进近红外($1\ \mu\text{m}$)波段超快光纤激光器的平均功率可达百瓦量级,单脉冲能量可达数百微焦量级^[27],但是由于元件性能较差以及技术不成熟等问题,基于 CPA 技术的高功率中红外光纤激光器^[24],无论是激光输出的平均功率还是单脉冲能量,都与先进的近红外超快激光器相差很远。

为解决中红外光纤激光器输出平均功率和单脉冲能量均较低的问题,本研究设计了一套三级中红外超快光纤激光系统,包括基于色散管理的中红外光纤激光振荡器和基于 CPA 技术的两级脉冲放大系统,以实现将现有中红外光纤激光器平均功率和脉冲能量均提升一个数量级。本研究通过对脉冲在各级系统中的演变进行数值模拟,深入分析各类非线性效应和增益效应对高能量宽谱脉冲的影响,优化系统整体设计、展宽器/压缩器色散设定和增益光纤长度等参数,最终实现大于 $10\ \text{W}$ 输出平均功率和 $250\ \text{nJ}$ 单脉冲能量的激光输出。

2 实验装置设计

为实现 $10\ \text{W}$ 、百纳焦量级的高功率中红外超快脉冲激光输出,本研究设计了包含三级结构的中红外光纤激光器系统,包括基于色散管理技术的超快中红外光纤激光振荡器(第一级)、基于 CPA 技术的超快光纤预放大器(第二级),以及基于 CPA 技术的光纤功率放大器(第三级)。图 1 为该系统的設計图。

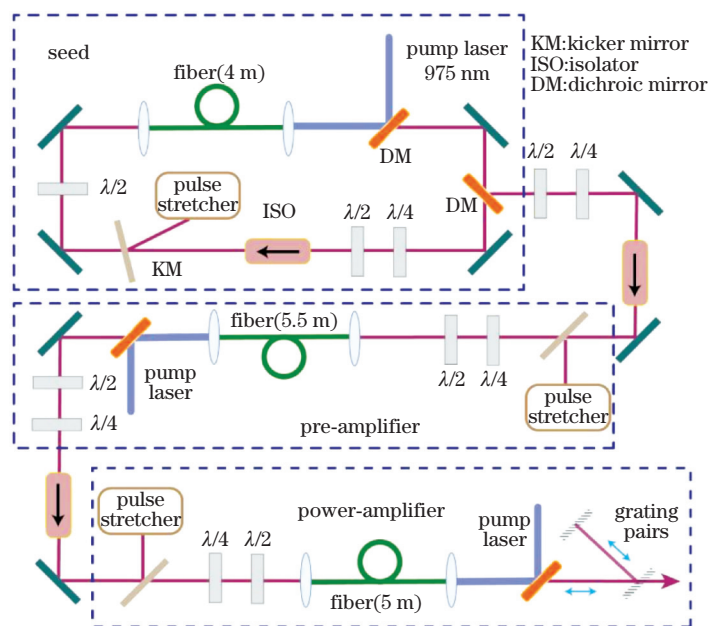


图 1 基于色散管理与啁啾脉冲放大技术的 $2.8\ \mu\text{m}$ 高功率超快光纤激光系统设计图

Fig. 1 Design of high-power ultrafast fiber laser system at $2.8\ \mu\text{m}$ using dispersion-management and CPA techniques

由于 ZBLAN 玻璃在 2.8 μm 波段具有较大的反常色散值,传统的 2.8 μm 锁模激光器一般工作在孤子脉冲状态,这使得超快振荡器输出的脉冲能量较小^[23-24],一般小于 5 nJ。为解决这一问题,在第一级超快脉冲振荡器的设计中引入能够提供大正色散量的中红外波段脉冲展宽器,以实现振荡器腔内的色散管理。当腔内总色散值为较大正色散时,激光器工作在耗散孤子区域,可在振荡器腔内得到较高能量(>10 nJ)的激光脉冲。

相较于近红外波段的激光输出,2.8 μm 波段的激光输出对光纤内离子掺杂浓度有着更高要求,以确保光纤有较强的增益能力^[28]。在实际实验中,所用到的 ZBLAN 光纤的掺杂浓度一般超过 0.01。本文的模拟参考了商用掺铒离子 ZBLAN 光纤的各项参数,其中,掺杂浓度为 0.07。因此,所提系统的设计没有考虑掺杂浓度对系统输出的影响,而是聚焦于色散对系统输出的影响。

在设计中,放大部分一共分为两级,如图 1 所示。在设计中之所以采用两级放大,而不是单一级的放大结构,是因为:从振荡器中输出的脉冲能量相对较小,单一级放大增益能力有限,为获得 10 W 以上激光输出,脉冲需要预放大至瓦量级;由于增益光纤具有较强的负色散,单脉冲能量较高时,孤子效应累积明显,脉冲会发生严重畸变,因此先将种子源脉冲进行时域展宽后再进行预放大。综合考虑光纤自身的增益能力与泵浦功率,分成两部分放大可以更加有效地利用光纤自身的增益能力,同时也可以避免泵浦端过高的泵浦功率导致的强烈热效应以及泵浦效率的降低。

第一级为预放大级,可将百毫瓦量级平均功率的种子激光输出放大至瓦量级;第二级是主功率放大级,将第一级放大器中瓦量级的激光输出放大至

10 W 量级。第一级预放大器采用 CPA 技术,展宽器提供的正色散要远大于光纤提供的负色散,保证增益光纤中较宽的脉冲宽度与较低的脉冲峰值功率,从而大大降低增益光纤中的非线性效应,从而保证放大过程中的脉冲质量。

主功率放大级同样采用 CPA 技术,采用正色散取值较大的展宽器,在时域上进一步展宽脉冲。在经过具有负色散增益光纤时,脉冲始终保持较大的正啁啾,从而保证在放大过程中脉冲的峰值功率较小,避免由非线性过高导致的脉冲畸变与高峰值功率下的光纤损坏。通过在增益光纤输出端引入光栅对脉冲压缩器进行啁啾补偿(图 1),可将脉冲宽度从皮秒量级压缩到数百飞秒量级。

3 种子源振荡器

超快激光种子源振荡器中的增益光纤长度为 4 m,这一光纤长度是综合考虑了光纤本身的增益能力、腔内能量的损耗以及输出的重复频率等因素,并结合了前期的实验结果给出的较为合适的设计长度。

若光纤长度过长,输出脉冲的重复频率将降低,进而导致输出平均功率降低;若光纤长度过短,输出脉冲的重复频率将升高,导致单脉冲能量下降,影响激光器锁模的自启动。若通过提高泵浦功率的方法来提升激光器锁模的自启动能力,则会产生过强的热效应,导致输出脉冲质量下降,甚至破坏光纤端面^[29]。

此外,振荡器中脉冲展宽器所引入的色散量为 +0.415 ps²,锁模激光振荡器的重复频率为 40 MHz。系统的其他参数如表 1 所示,其中超快种子源振荡器腔内的净色散量为 +0.081 ps²,属于较强的正色散,因此锁模振荡器工作在耗散孤子工作状态^[30-32]。

表 1 种子源振荡器参数设计

Table 1 Parameters in the simulation of seed oscillator

Device	Length /m	$\beta_2 / (\text{ps}^2 \cdot \text{km}^{-1})$	$\beta_3 / (\text{ps}^3 \cdot \text{km}^{-1})$	$\gamma / (\text{W}^{-1} \cdot \text{km}^{-1})$	Core diameter / μm	Concentration
Fiber	4	-83.5	0.64	0.24	15	0.07
Stretcher	1	415	-3.37	0		

可以使用广义非线性薛定谔方程来模拟脉冲在锁模振荡器腔内的运行:

$$\frac{\partial A(z, T)}{\partial z} = -\frac{\alpha}{2}A + i \sum_{k=2}^{\infty} \frac{i^k \beta_k}{k!} \frac{\partial^k}{\partial T^k} A + i\gamma \left(1 + \frac{i}{\omega_0} \frac{\partial}{\partial T} \right) \left[A \int_0^{\infty} R(\tau) |A(z, T-\tau)|^2 d\tau \right], \quad (1)$$

式中: $A(z, T)$ 为脉冲包络的复振幅; α 为传输过程中的线性损耗; β_k 为模传输函数的泰勒展开级数的第 k 项,它是各阶色散的表达形式; z 为传输距离; T 为传输时间; ω_0 为中心波长。(1)式等号右侧第三项包含了克尔非线性、脉冲内拉曼散射和自变陡效应,其中

$$R(\tau) = (1 - f_R)\delta(\tau) + f_R h_R(\tau), \quad (2)$$

式中： f_R 表示延迟拉曼响应对非线性极化的小数贡献； $h_R(\tau)$ 为由光场感应下分子振动决定的拉曼响应函数。

尽管在种子源振荡器中脉冲能量较低，峰值功率不高，导致脉冲内拉曼散射对于模拟结果的影响较小，但是脉冲在种子振荡器中需要进行多次循环，仍然不能忽略脉冲内拉曼散射的影响。拉曼响应函数可以近似表示为^[33]

$$h_R(\tau) = \frac{\tau_1^2 + \tau_2^2}{\tau_1 \tau_2} \exp(-\tau/\tau_2) \sin(\tau/\tau_1) \quad (3)$$

对于 ZBLAN 光纤来说， f_R 的取值为 0.2， $\tau_1 = 12.2$ fs， $\tau_2 = 32$ fs。

此外，在种子振荡器的模拟中还引入了用来描述光纤耦合、光栅衍射以及偏振元件产生损耗的部分。根据实验经验，模拟中设定通过脉冲展宽器的

光传输效率为 50%，由空间光路耦合至光纤的耦合效率为 60%。展宽器损耗主要来源于：1) 光栅衍射损耗，相较于近红外光栅，中红外光栅的效率较低；2) 与近红外波段相比，中红外波段展宽器内的光学器件效率也较低。

在数值模拟中，种子振荡器内的起始脉冲为高斯脉冲，脉冲能量为 4.5 nJ，脉冲宽度为 120 fs。通过将脉冲循环演变，可以模拟激光器腔中脉冲非线性传输过程，并记录脉冲在腔内不同区域的时频域上的演变过程。经过脉冲 100 圈的模拟过程，可得到自洽且稳定的锁模激光脉冲输出，前 100 圈稳定脉冲形成过程的模拟计算结果如图 2 所示。最终稳定的脉冲在振荡器输出端的能量为 10.3 nJ，脉冲宽度约为 1.4 ps，光谱宽度约为 50 nm，如图 2 所示。

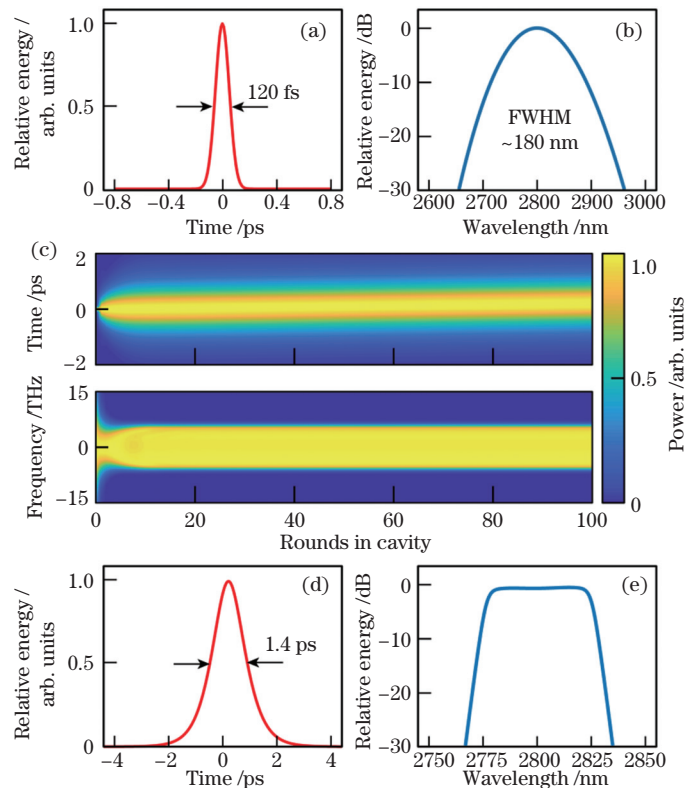


图 2 种子振荡器内脉冲时频域稳定演化。输入的初始高斯脉冲的(a)时域波形和(b)频域光谱；

(c)时域(上)与频域(下)的波形演化；腔内稳定脉冲的(d)时域波形和(e)频域光谱

Fig. 2 Wave shape transformation of the pulse in time domain and frequency domain in seed oscillator. (a) Time and (b) frequency domain wave shapes of input Gaussian pulse; (c) time (top) and frequency (below) transformation; (d)time and (e) frequency domain wave shapes of output pulse

从图 2 可以看到，脉冲在时域与频域上的形状在前 10 圈中快速变化，20 圈以后逐渐趋于稳定。值得注意的是，时域图像出现明显的倾斜，这是因为光纤中脉冲能量和频谱变化后，高阶色散和高阶非线性效应导致脉冲群速度变化。图 3 所示为种子源

振荡器在稳定脉冲形成后，单圈脉冲传输过程中时域与频域形状演化，以及最大与最小脉冲宽度。由图 3 可知，由于腔内的色散管理，脉冲在腔内始终保持较大的正啁啾运行，可有效降低脉冲在增益光纤中的非线性效应。腔内最小脉冲宽度约为 1.4 ps，

最大脉冲宽度约为 6.2 ps。从图 3(a)可以看出,稳定后的脉冲在腔内运转一圈,其频谱出现一定的变

化,这是由增益光纤内的增益光谱窄化效应与微弱的非线性光谱展宽效应之间的平衡造成的^[24]。

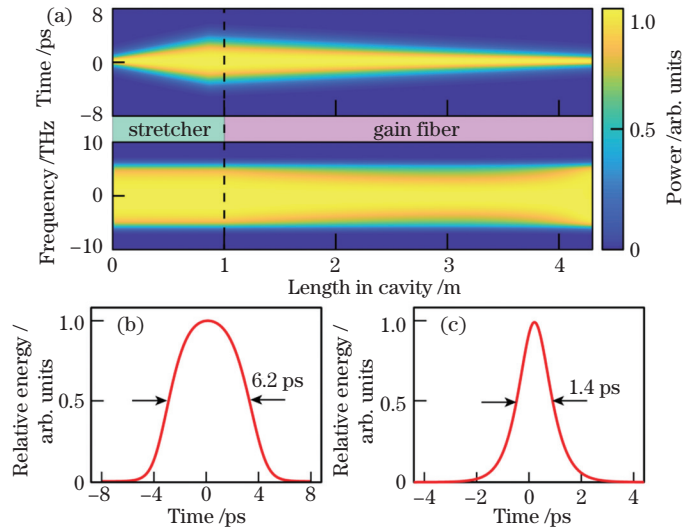


图 3 种子源振荡器在稳定脉冲形成后,单圈脉冲在传输过程中的时频域演化及脉冲宽度。

(a)时域与频域形状演化;(b)最大脉冲宽度;(c)最小脉冲宽度

Fig. 3 After forming a stable pulse in seed oscillator cavity, transmission process of a single round pulse in time and frequency domain and pulse widths. (a) Transformation process of pulse shape and spectral shape; (b) the largest pulse width; (c) the smallest pulse width

4 光纤预放大器

预放大器部分采用了类似 CPA 结构。值得注意的是,与典型的 CPA 结构相比,本设计中没有采用独立的脉冲压缩单元。脉冲先经过一段较强的正色散脉冲展宽器,然后时域上被展宽的脉冲被送入掺铒 ZBLAN 增益光纤中。预放大器中没有在增益光纤后设置压缩器,这是因为带有一定正色散量的脉冲更有利于在下一级主功率放大器中进行低非线性效应增强。在此预放大级,带有正啁啾的脉冲经过具有反常色散值的增益光纤,一部分脉冲正啁啾被补偿,因此脉冲的时域宽度在增益放大过程中不断变短。此预放大器的参数设计如表 2 所示。

表 2 预放大器部分参数设计

Table 2 Parameters in the simulation of pre-amplifier

Device	Length / m	$\beta_2 / (\text{ps}^2 \cdot \text{km}^{-1})$	$\beta_3 / (\text{ps}^3 \cdot \text{km}^{-1})$	$\gamma / (\text{W}^{-1} \cdot \text{km}^{-1})$
Fiber	5.5	-83.5	0.64	0.24
Stretcher	1	800	-6.5	0

在激光从种子源振荡器传输到预放大器部分的过程中,光束经过输出耦合的双色镜、偏振片与光隔离器等器件过程中会损失一部分能量,因此从腔内光纤中只有一部分能量会进入预放大器部分。根据实验经验,预放大器的输出能量大约是增益光纤中的 30%;其他部分的损耗与种子源振荡器一样。脉

冲在预放大器中传输的模拟结果如图 4 所示,脉冲被展宽器放大到 10.3 ps,增益光纤中较强的负色散会在时域上对脉冲进行一定程度的压缩。由于在此预放大器设计中,展宽器引入的正色散量远大于增益光纤提供的负色散量,因此从此预放大器输出的脉冲仍然具有一定的正色散量,脉冲宽度为 3.4 ps。在脉冲频谱上,由于增益光纤内的增益光

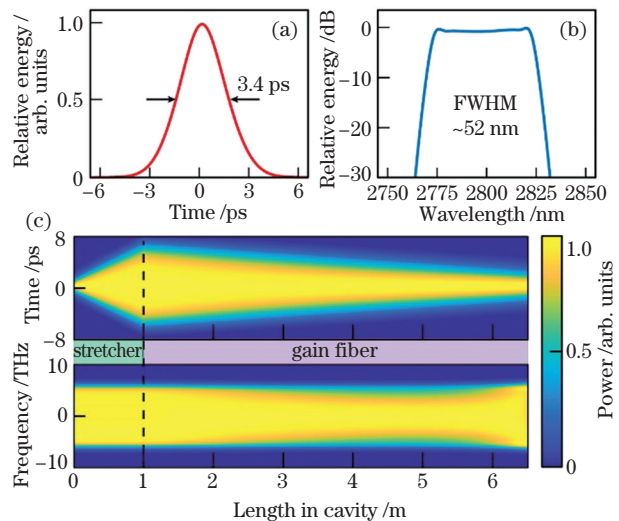


图 4 预放大器内的脉冲输出。(a)脉冲时域波形;(b)脉冲光谱;(c)时域与频域的演化过程

Fig. 4 Output pulse from the pre-amplifier. (a) Pulse shape; (b) pulse spectrum; (c) transformation process in time and frequency domain

谱窄化效应与非线性展宽效应平衡,输出脉冲的频谱宽度与输入脉冲相比变化不大,约为 52 nm,如图 4 所示。最终输出的单脉冲能量约为 64 nJ,激光平均功率约为 2.5 W。

5 主功率放大级及其参数优化

主功率放大级中由于脉冲能量与激光平均功率相较于预放大器要高约一个量级,因此采用传统的 CPA 结构设计。在进入增益光纤之前,需采用正色散量更大的脉冲展宽器实现更强的脉冲时域展宽,尽量减小脉冲峰值功率,从而有效降低增益光纤中的非线性效应,并尽量避免高功率激光对光纤端面的破坏。在主功率放大器中,增益光纤的长度选为 5 m,由于从增益光纤输出的激光平均功率在 10 W 量级,当脉冲重复频率为 40 MHz 时,对应的增益光纤内最大单脉冲能量可达数百纳焦。在如此高的单脉冲能量下,无法采用文献[24]中的瓦量级放大器设计。即当增益光纤前的脉冲展宽器引入的脉冲正啁啾和增益光纤所引入的脉冲负啁啾相互匹

配时,虽然在较低平均功率、较低单脉冲能量运转下,可以从增益光纤中直接输出百飞秒量级的超快脉冲,避免了增益光纤之后额外的脉冲压缩器(啁啾补偿单元)的使用,但是在较高的平均功率与单脉冲能量下,此种方案必然导致增益光纤末端存在较短的脉冲宽度与极高的脉冲峰值功率,从而导致脉冲在增益光纤内产生较强的非线性效应,导致时域与频域上的波形产生畸变,如图 5 所示。当主功率放大器中的脉冲展宽器引入的色散量设置为 $+0.65 \text{ ps}^2$ 时,此时只依靠增益光纤的反常色散压缩脉冲,由于光纤内的脉冲峰值功率过高,非线性效应会极大地影响输出脉冲的脉冲质量。如图 5 所示,当输出能量提高到约 250 nJ 时(对应的激光平均功率约 10 W),脉冲在时域和频域上都产生了较强的非线性畸变。在时域上,脉冲中心部分的能量占比很低,绝大多数能量集中在脉冲较宽的基座部分,如图 5(a)所示;同时,由于增益光纤内存在较大的非线性效应,脉冲光谱形状发生严重的畸变,如图 5(b)所示。

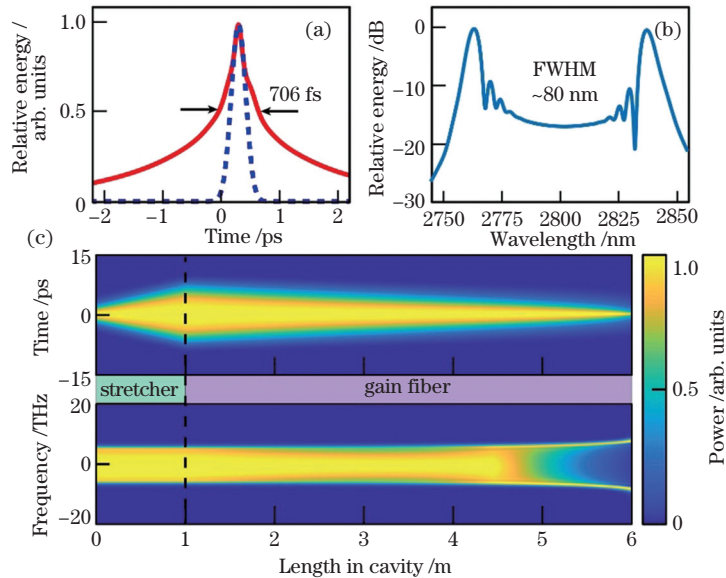


图 5 当脉冲展宽器所提供的正啁啾与增益光纤所提供的负啁啾平衡时,主功率放大器内的脉冲输出。

(a) 脉冲波形; (b) 脉冲光谱; (c) 时域与频域的演化过程

Fig. 5 Output pulse in the main amplifier without compressor when positive chirp provided by pulse stretcher is balanced by negative chirp provided by gain fiber. (a) Pulse shape; (b) pulse spectrum; (c) transformation process in time and frequency domain

为减小主功率放大器中输出脉冲的非线性畸变,并进一步提升放大器的平均功率与单脉冲能量输出水平,应进一步提高主功率放大器中脉冲展宽器正色散量的取值,并在增益光纤后利用一个高功率脉冲压缩器来补偿放大后脉冲中残余的正啁啾,从而窄脉的时域宽度,提升脉冲的峰值功率。由于所设计的

系统新增了脉冲压缩器,它会引入一些损耗,从而降低激光系统输出功率的能力。为缓解这个问题,此处的脉冲压缩器采用 Treacy 光栅对方案^[34],优化光栅中红外波段性能和入射角度,可最大限度地减小压缩器损耗,实现超过 60% 的整体效率,使得单个脉冲能量超过 250 nJ,平均功率大于 10 W。数值

模拟结果表明,主功率放大器的色散量至少要达到 $+0.85 \text{ ps}^2$, 才能实现较低的非线性脉冲畸变。在研究中,调节脉冲展宽器的色散量在 $0.85 \sim 1.40 \text{ ps}^2$ 范围内,通过一系列模拟实验,计算出在 250 nJ 固定输出单脉冲能量, 10 W 输出激光平均功率条件下,不同展宽器正色散量下从增益光纤输出的脉冲宽度和中心脉冲能量占比如图 6 所示。

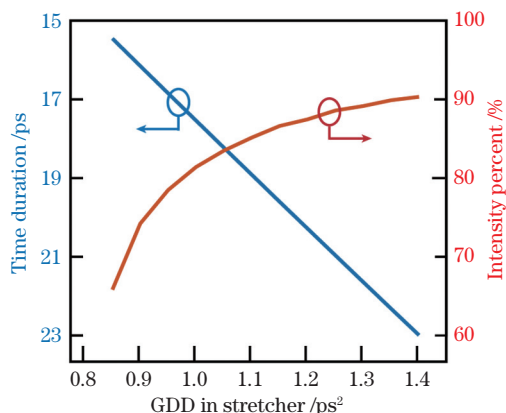


图 6 增益光纤输出脉冲宽度、中心部分能量占比随展宽器提供的正色散的变化

Fig. 6 Change of fiber output pulse width and the proportion of central pulse energy with normal dispersion provided by stretcher

由图 6 可知:当展宽器的正色散量较小时,增益光纤中输出脉冲时域宽度较小,但非线性效应较强,脉冲畸变较大,导致通过压缩器进行脉冲压缩以后,

较多能量会分散到脉冲基底上,脉冲中心部分能量占比较低;相反,当展宽器的正色散量较大时,中心脉冲能量占比超过 85%,时域脉冲宽度较宽。对于输出脉冲,一个重要的评价指标是其中中心脉冲占比,在多数非线性效应的应用中,中心脉冲能量代表了脉冲的主要作用能量;另外,中心能量占比较小时,脉冲在非线性放大过程中发生显著畸变,脉冲质量下降,并存在较多的不可压缩啁啾,导致尽管脉冲频域宽度很大,但时域宽度并没有显著压缩,峰值功率并不会明显提升,如图 5 所示。

如图 7 所示,为了更好地分析脉冲随正色散值的变化规律,选取两个正二阶色散取值 ($+0.85 \text{ ps}^2$ 、 $+1.25 \text{ ps}^2$) 进行比较。在模拟中,展宽器和压缩器都被视作 1 m 长无非线性效应的光纤。增益光纤长度为 5 m ,其他光纤参数与系统损耗设置与预放大级一致,两组模拟实验的输出脉冲能量都为 250 nJ 。表 3 所示为两种情况的展宽器与压缩器的色散取值。

表 3 两组不同的主放大器模拟参数的选择

Table 3 Two different groups of parameters of main amplifier chosen for the simulation

Device	GDD / ps^2	$\beta_2 / (\text{ps}^2 \cdot \text{km}^{-1})$	$\beta_3 / (\text{ps}^3 \cdot \text{km}^{-1})$
Stretcher		850	-6.91
Compressor	+0.730	-120	0.98
Stretcher		1250	-10.16
Compressor	+0.632	-618	5.02

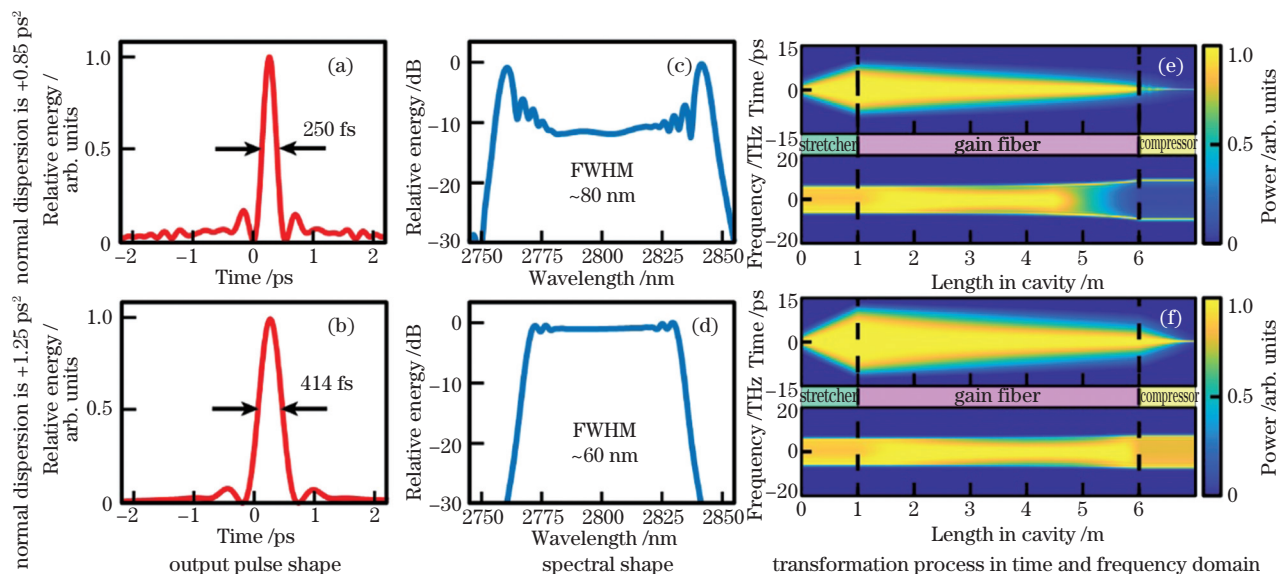


图 7 两种不同色散取值下主放大器内的脉冲输出

Fig. 7 Output pulse in the main amplifier with two different groups dispersion values

从图 7(a)、(c)可以看到:当展宽器提供的正色散比较低时,由于脉冲展宽的宽度较小(约 250 fs),非线性效应强烈,导致脉冲时域、频域形状发生一定程度

的畸变,脉冲基底能量变大,中心脉冲能量占比不足 70%,从而导致脉冲宽度变窄,但压缩后峰值功率并无明显提高。当提供的正色散量比较大时,压缩后脉

冲的宽度较大(约 414 fs),但放大过程中脉冲在时域上的展宽量较大,可有效抑制非线性效应,使得脉冲在时域、频域上的形状不会产生明显畸变。此外,正色散量比较大时中心脉冲的占比也相应地提高了(约 90%),脉冲峰值功率达到 460 kW,其中心脉冲能量显著大于正色散较低的情况。另外,在实际实验中,受限于光学元件尺寸等,展宽器引入的色散量越大,设计难度越高,因此正色散量不应太大。以上研究结果表明,为获得高质量、高能量的中红外脉冲,在 CPA 放大过程中展宽器应引入较大的正色散($>1.25 \text{ ps}^2$),使得非线性效应能够被有效地抑制,确保接近 90%的脉冲能量集中在中心脉冲区域,同时也能保证压缩后的脉冲拥有相对较高的峰值功率。

6 总 结

设计了一套基于掺铒 ZBLAN 光纤的 $2.8 \mu\text{m}$ 中红外高功率超快光纤激光系统。为了提高中红外超快光纤激光的平均功率与单脉冲输出能量,系统包含种子源振荡器与两级放大器,通过优化系统内多个脉冲展宽器与压缩器的参数设计,有效降低了两级放大过程中增益光纤内的非线性效应,从而实现约 400 fs 脉冲宽度、10 W 量级平均功率、近兆瓦量级峰值功率的中红外超快光纤激光输出。此外,本研究详细讨论了种子源振荡器和预放大器中的超快脉冲演化过程,以及主放大级中展宽器与压缩器的不同色散量对最终输出脉冲能量和输出质量的影响,为下一阶段在实验室搭建高功率、中红外超快光纤激光系统提供参考。

参 考 文 献

- [1] Pantawane M V, Robertson W B, Khan R J K, et al. Fundamentals of three-dimensional Yb-fiber Nd:YAG laser machining of structural bone[J]. *Journal of Applied Physics*, 2019, 126(12): 124901.
- [2] Amini-Nik S, Kraemer D, Cowan M L, et al. Ultrafast mid-IR laser scalpel: protein signals of the fundamental limits to minimally invasive surgery[J]. *PLoS One*, 2010, 5(9): e13053.
- [3] Waynant R W, Ilev I K, Gannot I. Mid-infrared laser applications in medicine and biology[J]. *Philosophical Transactions of the Royal Society of London Series A*, 2001, 359(1780): 635-644.
- [4] Popa D, Udrea F. Towards integrated mid-infrared gas sensors[J]. *Sensors*, 2019, 19(9): 2076.
- [5] Chen J, Nitta K, Zhao X, et al. Adaptive-sampling near-Doppler-limited terahertz dual-comb spectroscopy with a free-running single-cavity fiber laser [J]. *Advanced Photonics*, 2020, 2(3): 036004.
- [6] Haas J, Mizaikoff B. Advances in mid-infrared spectroscopy for chemical analysis [J]. *Annual Review of Analytical Chemistry*, 2016, 9(1): 45-68.
- [7] Schliesser A, Picqué N, Hänsch T W. Mid-infrared frequency combs[J]. *Nature Photonics*, 2012, 6(7): 440-449.
- [8] Hugi A, Terazzi R, Bonetti Y, et al. External cavity quantum cascade laser tunable from 7.6 to 11.4 μm [J]. *Applied Physics Letters*, 2009, 95(6): 061103.
- [9] Thompson N R, Dunning D J, Clarke J A, et al. First lasing of the ALICE infra-red free-electron laser [J]. *Nuclear Instruments and Methods in Physics Research Section A*, 2012, 680: 117-123.
- [10] Whittaker K E, Ciaffoni L, Hancock G, et al. A DFG-based cavity ring-down spectrometer for trace gas sensing in the mid-infrared[J]. *Applied Physics B*, 2012, 109(2): 333-343.
- [11] Leindecker N, Marandi A, Byer R L, et al. Broadband degenerate OPO for mid-infrared frequency comb generation[J]. *Optics Express*, 2011, 19(7): 6296-6302.
- [12] Li B W, Wu J M, Xu M H, et al. Study on widely tunable mid-infrared difference-frequency generation based on passive synchronization [J]. *Chinese Journal of Lasers*, 2020, 47(11): 1115001.
李博文, 武佳美, 徐明航, 等. 基于被动同步的宽调谐中红外差频技术研究[J]. *中国激光*, 2020, 47(11): 1115001.
- [13] Maine P, Strickland D, Bado P, et al. Generation of ultrahigh peak power pulses by chirped pulse amplification [J]. *IEEE Journal of Quantum Electronics*, 1988, 24(2): 398-403.
- [14] Wang P, Huang J P, Xie S R, et al. Broadband mid-infrared supercontinuum generation in dispersion-engineered As_2S_3 -silica nanospire waveguides pumped by 2.8 μm femtosecond laser[J]. *Photonics Research*, 2021, 9(4): 630-636.
- [15] Wang F, Pistore V, Riesch M, et al. Ultrafast response of harmonic modelocked THz lasers [J]. *Light: Science & Applications*, 2020, 9: 51.
- [16] Wang F H, Maussang K, Moumdji S, et al. Generating ultrafast pulses of light from quantum cascade lasers[J]. *Optica*, 2015, 2(11): 944-949.
- [17] Feng X, Shi J, Segura M, et al. Halo-tellurite glass fiber with low OH content for 2-5 μm mid-infrared nonlinear applications[J]. *Optics Express*, 2013, 21(16): 18949-18954.
- [18] Jia Z X, Yao C F, Li Z R, et al. Progress on novel high power mid-infrared fiber laser materials and supercontinuum laser[J]. *Chinese Journal of Lasers*, 2019, 46(5): 0508006.

- 贾志旭, 姚传飞, 李真睿, 等. 新型高功率中红外光纤激光材料与超连续谱激光研究进展[J]. 中国激光, 2019, 46(5): 0508006.
- [19] Xia C, Kumar M, Kulkarni O P, et al. Mid-infrared supercontinuum generation to 4.5 microm in ZBLAN fluoride fibers by nanosecond diode pumping [J]. Optics Letters, 2006, 31(17): 2553-2555.
- [20] Sanghera J S, Shaw L B, Aggarwal I D. Chalcogenide glass-fiber-based mid-IR sources and applications[J]. IEEE Journal of Selected Topics in Quantum Electronics, 2009, 15(1): 114-119.
- [21] Dai S X, Wang M, Wang Y Y, et al. Review of mid-infrared supercontinuum spectrum generation based on chalcogenide glass fibers [J]. Laser & Optoelectronics Progress, 2020, 57(7): 071603.
戴世勋, 王敏, 王莹莹, 等. 基于硫系玻璃光纤的中红外超连续谱产生研究进展[J]. 激光与光电子学进展, 2020, 57(7): 071603.
- [22] Aydin Y O, Fortin V, Vallée R, et al. Towards power scaling of 2.8 μm fiber lasers [J]. Optics Letters, 2018, 43(18): 4542-4545.
- [23] Qin Z P, Xie G Q, Gu H, et al. Mode-locked 2.8- μm fluoride fiber laser: from soliton to breathing pulse[J]. Advanced Photonics, 2019, 1(6): 065001.
- [24] Huang J, Pang M, Jiang X, et al. Sub-two-cycle octave-spanning mid-infrared fiber laser[J]. Optica, 2020, 7(6): 574-579.
- [25] Duval S, Gauthier J C, Robichaud L R, et al. Watt-level fiber-based femtosecond laser source tunable from 2.8 to 3.6 μm [J]. Optics Letters, 2016, 41(22): 5294-5297.
- [26] Tegin U, Rahmani B, Kakkava E, et al. Single-mode output by controlling the spatiotemporal nonlinearities in mode-locked femtosecond multimode fiber lasers[J]. Advanced Photonics, 2020, 2(5): 056005.
- [27] Eidam T, Rothhardt J, Stutzki F, et al. Fiber chirped-pulse amplification system emitting 3.8 GW peak power[J]. Optics Express, 2010, 19(1): 255-260.
- [28] Pollnau M, Spring R, Ghisler C, et al. Efficiency of erbium 3- μm crystal and fiber lasers[J]. IEEE Journal of Quantum Electronics, 1996, 32(4): 657-663.
- [29] Huang J, Pang M, Jiang X, et al. Route from single-pulse to multi-pulse states in a mid-infrared soliton fiber laser [J]. Optics Express, 2019, 27(19): 26392-26404.
- [30] Shen Y, Wang Y, Chen H, et al. Wavelength-tunable passively mode-locked mid-infrared Er^{3+} -doped ZBLAN fiber laser [J]. Scientific Reports, 2017, 7(1): 14913.
- [31] Antipov S, Hudson D D, Fuerbach A, et al. High-power mid-infrared femtosecond fiber laser in the water vapor transmission window[J]. Optica, 2016, 3(12): 1373.
- [32] Song Y F, Wang Z H, Wang C, et al. Recent progress on optical rogue waves in fiber lasers: status, challenges, and perspectives [J]. Advanced Photonics, 2020, 2(2): 024001.
- [33] Blow K J, Wood D. Theoretical description of transient stimulated Raman scattering in optical fibers [J]. IEEE Journal of Quantum Electronics, 1989, 25(12): 2665-2673.
- [34] Treacy E. Optical pulse compression with diffraction gratings[J]. IEEE Journal of Quantum Electronics, 1969, 5(9): 454-458.

Design of a 10 W Level Dispersion-Managed High-Power Ultrafast Mid-Infrared Fiber Laser System

Sun Weiyi^{1,5}, Huang Jiapeng^{1,2,4*}, Chen Liming², Huang Zhiyuan¹, He Wenbin²,
Jiang Xin^{2,3}, Pang Meng^{1,2,3**}, Leng Yuxin^{1,3***}

¹ State Key Laboratory of High Field Laser Physics, Shanghai Institute of Optics and Fine Mechanics, Chinese Academy of Sciences, Shanghai 201800, China;

² Innovation and Integration Center of New Laser Technology, Shanghai Institute of Optics and Fine Mechanics, Chinese Academy of Sciences, Shanghai 201800, China;

³ School of Physics and Opto-Electronic Engineering, Hangzhou Institute for Advanced Study, Chinese Academy of Sciences, Hangzhou, Zhejiang 310013, China;

⁴ Department of Electrical Engineering, Hong Kong Polytechnic University, Hong Kong, China;

⁵ School of Physical Science and Technology, Shanghai Tech University, Shanghai 201210, China

Abstract

Objective Mid-infrared (mid-IR) fiber lasers have important applications in gas spectroscopy, material processing,

laser surgery, and other fields, since several molecular vibrational absorption bands reside in the mid-IR “fingerprint” region, boosting the strength of light-matter interaction by more than one order of magnitude. However, it is challenging to develop high-performance mid-IR ultrafast sources, because both electrical and optical components at mid-IR wavelengths are far from maturity. In recent years, both continuous-wave (CW) and pulsed lasers in the mid-IR region have been successfully demonstrated, based on several laser techniques, which provide useful means of generating high-power pulses. In the field of mid-IR fiber laser systems, for example, one of the most widely-used gain materials is the ZBLAN ($\text{ZrF}_4\text{-BaF}_2\text{-LaF}_3\text{-AlF}_3\text{-NaF}$) fiber, which shows several advantages, such as long-term stability, and high-power capability. With different doping rare-earth ions, stable lasing, ranging from $2\ \mu\text{m}$ to $4\ \mu\text{m}$, has been reported in this type of gain fiber in room temperature. ZBLAN fibers doped with Er^{3+} ions are the most widely-used, with two radiation wavelengths ($2.8\ \mu\text{m}$ and $3.5\ \mu\text{m}$): they can be efficiently pumped with well-developed 980 nm high-power laser diodes, with a maximum power output of $\sim 40\ \text{W}$ under CW operation. However, due to the limit of fiber nonlinearity, the highest output power for ultrafast mid-IR laser is at a Watt level, thus restricting practical applications of such laser systems. In this paper, we design a high-power ultrafast fiber laser system at $2.8\ \mu\text{m}$ with a multi-stage scheme, in order to boost the laser output power by an order of magnitude comparing to the best results ever-reported. Our design is based on rigorous numerical simulations, solving the non-linear Schrodinger equation (NLSE) of the pulse spectra-temporal evolution under different amplification conditions. Results demonstrated here can provide references for designing and constructing high-power ultrafast mid-IR fiber laser systems.

Methods In the present research, we apply the seed oscillator, a dispersion-managed mode-locked fiber laser. Using split-step Fourier method, we are able to apply NLSE to simulate pulse propagation, under different nonlinear and dispersive sections. To obtain enough gain and high-power outputs over 10 W, we designed the laser system as composed by three stages: seed oscillator, pre-amplifier, and main amplifier. After the pre-amplifier stage, we obtained high-quality laser pulse with smooth spectral and temporal profiles, by gradually changing the dispersion values in both the seed oscillator and the pre-amplifier. In the main amplifier, we introduced chirped-pulse amplification (CPA) method to mitigate non-linear pulse distortions, which mainly originate from interplays between strong nonlinearity, gain effects, and dispersion. We analyzed the laser output performances of the compressor and the stretcher at different settings in the CPA set-up. By choosing two different groups of stretcher settings, and comparing the resulting laser performances, including output power, pulse width, spectral width, and pulse shape, we were able to optimize the design of the CPA system.

Results and Discussions With the help of the systematic simulation and optimization, we obtained output pulses from the seed oscillator with $\sim 10\ \text{nJ}$ pulse energies, and several-ps pulse durations (Figs. 2 and 3). These output pulses were amplified in the pre-amplifier stage by an order of magnitude, with tens of nJ pulse energies and several-pJ level pulse durations (Fig. 4). In order to analyze the performance of the third stage of the main amplifier, we firstly compared two different amplifier designs: one is the conventional CPA scheme, in which the chirped pulses output of the gain fiber were launched into a compressor; the dispersion value of the stretcher was carefully selected to match the gain fiber length, so as to avoid the use of pulse compressor after the gain fiber. In the second scheme, strong pulse distortions due to excessive nonlinearity in the gain fiber were observed when the amplified pulse energy reached $\sim 250\ \text{nJ}$, leading most pulse energies to be located within pulses’ pedestals (Fig. 5). In contrast, by using the conventional CPA scheme, high-quality amplified pulses with both higher pulse energies and peak powers can be obtained at the output port of the main amplifier stage. In our studies, different normal dispersion values of the stretcher in the main amplifier stage, ranging from $0.85\ \text{ps}^2$ to $1.40\ \text{ps}^2$, were used to optimize the design of this stage. To evaluate the results, we examined the pulse duration, bandwidth, peak power, and temporal shape of the output pulses from the main amplifier at different settings. When keeping the output power of the main amplifier, we obtained anomalous dispersion values provided by the compressor under different normal dispersion values when the energy located in the pedestal was the smallest. Meanwhile, other parameters, such as the pulse bandwidth, and output power, have been recorded. We found that, under the same average power, the quality of the output pulse increases as the normal dispersion value of the stretcher increases (Fig. 6). Finally, two normal dispersion values ($0.85\ \text{ps}^2$ and $1.25\ \text{ps}^2$) have been chosen to investigate the spectral distortion, which is directly impacted by the counterbalance, between self-phase modulation and gain-narrowing effect. Although the pulse duration under $0.85\ \text{ps}^2$ is shorter, the proportion of central pulse is smaller, and the shape of pulse spectrum appears worse than those under $1.25\ \text{ps}^2$ (Fig. 7): this is mainly caused by the combined effect of nonlinearity and gain-narrowing effect

in the gain fiber. When the pulse has smaller bandwidth, the pulse peak power is stronger when propagating in the gain fiber and the Kerr effect would also be stronger, while the gain-narrowing effect prevents the broadening of the pulse. Due to these reasons, both temporal and spectral shapes of the amplified pulse were highly distorted by the excessive nonlinearity in the gain fiber.

Conclusions In summary, we have demonstrated the design of a three-stage ultrafast mid-IR fiber laser system, which can directly deliver 10 W level average power, hundreds of nJ pulse energy, and hundreds of fs pulse duration. We believe that the design and analysis demonstrated here can provide useful information to the construction and optimization of real high-power, ultrafast, mid-IR fiber laser systems.

Key words lasers; mid-infrared laser; mode-locked fiber lasers; chirped-pulse amplification; high-power pulse laser